JOURNAL OF THERMOPHYSICS AND HEAT TRANSFER
Vol. 21, No. 2, April–June 2007

Calculation of Thermal Response of Ablator Under Arcjet Flow Condition

Toshiyuki Suzuki*
Japan Aerospace Exploration Agency, Tokyo 182-0012, Japan
Takeharu Sakai†
Nagoya University, Aichi 464-8603, Japan
and
Tetsuya Yamada‡
Japan Aerospace Exploration Agency, Kanagawa 229-8510, Japan

DOI: 10.2514/1.25499

An integrated computational method is developed to calculate thermal response of ablator under an arcjet flow condition. In the method, the arcjet freestream condition in the test section is evaluated by calculating the flows in the arcjet wind tunnel fully theoretically. The thermal response of the ablator is calculated by loosely coupling the shock layer computational fluid dynamics code and the 2-D version of ablation code using the arcjet freestream condition so evaluated. The method is applied to the heating tests conducted in the 1 MW arcjet wind tunnel for one operating condition. The influence of catalytic conditions of ablating surface and the effect of nitridation reaction and surface roughness on the thermal response of the ablator are investigated. Comparison of the temperature profile at the ablating surface between calculation and measurement suggests that the measured temperature profile can be reproduced with a low catalytic efficiency of the surface. It is found that the nitridation reaction increase the surface temperature moderately, and that the effect of the roughness on the surface were small for the present operating condition.

Nomenclature

A	=	cell area, m^2
A_k	=	static weight for component k
B_k	=	activation temperature for component k, K
c_p	=	specific heat at constant pressure, $J/(kg \cdot K)$
c_s	=	mass fraction of species s
e	=	internal energy, J/kg
f_k	=	collision frequency for component k, s^{-1}
H_0	=	formation enthalpy, J/kg
J	=	mass flux, $kg/(m^2 \cdot s)$
k	=	surface reaction velocity, m/s
M_s	=	molecular weight of species s, kg/mol
$\dot{m}_g$	=	pyrolysis gas mass flux, $kg/(m^2 \cdot s)$
p_s	=	partial pressure of species s, Pa
q	=	heat flux, W/m^2
R	=	pyrolysis rate, $kg/(m^3 \cdot s)$
$\bar{R}$	=	universal gas constant, 8.314 $J/(mol \cdot K)$
r_c	=	mass loss rate, m/s
S	=	recession, m
T	=	temperature, K
α	=	reaction probability in Eqs. (4), (5), and (8) or catalytic efficiency in Eqs. (9–12)
ε	=	surface emissivity
κ	=	thermal conductivity, $W/(m \cdot K)$
μ_k	=	reaction order for component k
ρ	=	density, kg/m^3
σ	=	Stefan–Boltzmann constant, $W/(m^2 \cdot K^4)$

Subscripts

c	=	char state
cat_s	=	catalytic recombination of species s
g	=	pyrolysis gas
nit	=	nitridation
oxi	=	oxidation
r	=	resin
s	=	solid state
sub	=	sublimation
v	=	virgin state
vib	=	vibrational–electronic mode
w	=	wall

I. Introduction

IN JAPAN, there has been an increasing interest for planetary entry missions. Examples are sample return mission named HAYABUSA (MUSES-C) [1] and unmanned space experiment recovery system (USERS).§ In these missions, a carbon fiber reinforced plastic (CFRP) ablator was chosen as the material of a thermal protection system (TPS). The test pieces of CFRP ablators were tested in arcjet wind tunnels to examine the thermal and mechanical performance of the ablators for a predicted flight environment. In the heating tests, several data to quantify the thermomechanical performance of the ablator were measured. The data were used to design the heatshield to withstand the heating environment during an entry flight. However, because the arcjet test conditions were not well characterized, the obtained data could not be reliably extrapolated to the flight environment. As a result, the heatshield was designed with a large safety factor.

To reduce such a safety factor, current capabilities need to be improved in evaluating the performance of ablating heatshield

Presented as Paper 778 at the 44th AIAA Aerospace Sciences Meeting and Exhibit, Reno, NV, 9–12 January 2006; received 30 May 2006; revision received 20 October 2006; accepted for publication 29 November 2006.

*Postdoctoral Fellow, Institute of Aerospace Technology, 7-44-1 Jindaiji Higashi-machi, Chofu-shi; suzuki.toshiyuki@jaxa.jp. Member AIAA.
†Assistant Professor, Department of Aerospace Engineering, Furo-cho, Chikusa-ku, Nagoya. Member AIAA.
‡Research Associate, Institute of Space and Astronautical Science, 3-1-1 Yoshinodai, Sagamihara-shi. Member AIAA.

§Data available online at http://www.usef.or.jp/English/f3_project/users/f3_users.html [cited 12 March 2006].

materials in arcjet tests. One of the important capabilities to be improved will be a theoretical method in calculating the thermal response of the ablator in an arcjet flow. Three major requirements are given as follows:

1) We need to know the thermal response within a CFRP ablator. The CFRP ablator consists of a base carbon fiber and a resin. When the virgin material of the ablator is heated, the resin decomposes and a pyrolysis gas including carbonaceous and hydrocarbon species is formed within the ablator. The pyrolysis gas then flows toward a wall surface and is released into the boundary layer. We need to account for this pyrolysis phenomenon by solving a set of conservation equations. In addition, the radius of the test piece used in an arcjet testing is usually so small that the influence of the heat input from the sidewall of the test piece is no longer negligible. For such a case, the thermal response of ablator should be treated two-dimensionally.

2) We need to know the flowfield properties over the ablator. Because the thermochemical state in the boundary layer is affected by the injection of the pyrolysis gas, the heating environment of the ablator is modified. This modification in turn affects the thermal response of the ablator. Furthermore, atomic oxygen and nitrogen in the boundary layer will reach the ablating surface. Because the ablating surface becomes nearly pure carbon due to the pyrolysis process, the solid carbon on the surface is oxidized or nitrided by the atomic oxygen and nitrogen in the arcjet freestream. As a result, the material surface recedes and the mass of the material reduces. In addition, because the surface shape of ablator is changed, the heat flux distribution over the ablating surface varies with time. Therefore, we need to introduce coupling between flowfield and the thermal response of the ablator. For the flowfield calculation, carbonaceous species produced by ablation must be included in addition to air species to account for the thermochemical nonequilibrium state of the mixture of the gas.

3) We need to know the arcjet freestream condition. The arcjet flow is heated to a high enthalpy condition through an electric discharge and thus the flow is highly dissociated and ionized. When the arcjet flow is expanded through nozzle, density is so low that the recombination process is not completed. Therefore, the concentration of the atomic species in the arcjet freestream is greater than that calculated by the equilibrium relationship. This amount of the atomic species needs to be known. In addition, because the centerline region of the arcjet freestream is used for the testing of the ablator test piece, in which the flow properties are nearly constant in radial direction, the thermochemical state of the arcjet flow in this centerline region must be determined. To the best of our knowledge, there have been no prior attempts to calculate the ablating environment accounting for all these aspects.

Our recent independent efforts enable us to make a theoretical prediction of the ablating environment under an arcjet condition. To calculate the thermal response within an ablator, Ahn et al. developed a computer code named Super Charring Materials Ablation (SCMA) [2]. Unlike the well-known Charring Materials Ablation (CMA) code [3], the SCMA solves the motion of the pyrolysis gas in addition to the heat conduction inside the ablating material. Recently, Suzuki et al. developed a thermochemical nonequilibrium computational fluid dynamics (CFD) code that accounts for 21 chemical species including carbon compounds [4]. In that work, an aerodynamic heating environment over the MUSES-C capsule was calculated by integrating the developed CFD code and the SCMA code. It was found out that converged solutions can be obtained by loosely coupling the CFD code and the SCMA code within a few iterations. In the sequel work, for the purpose of studying the thermal response of ablator that is put into arcjet flow, the SCMA code was extended to a 2-D version by Suzuki et al. [5]. The updated code named SCMA2 is able to calculate the thermal conduction and the motion of pyrolysis gas in 2-D space.

Sakai and Olejniczak developed a computational code that calculates the entire flowfield from upstream end of the arc heater to nozzle exit in a segmented-constrictor type arc-heated wind tunnel [6,7]. The flow from the upstream electrode chamber to the nozzle throat is solved using a newly developed arc-heater flowfield code named ARCFLO3 which accounts for Joule heating and radiative transfer phenomena in the arc heater. The downstream region of the nozzle beyond the throat is described by thermochemical nonequilibrium Navier–Stokes equations using the flow properties at the nozzle throat obtained by the ARCFLO3 calculation as an inflow condition [8].

By integrating these computational codes, it seems possible now to conduct a detailed calculation of the ablating environment under an arcjet flow condition.

The present study aims to establish an integrated computational methodology that can analyze thermal response of ablator under arcjet flow condition. For this purpose, we try to simulate the ablating environment by integrating the independent computational techniques: the SCMA2 code is used for the ablation analysis, flowfield is calculated using the thermochemical nonequilibrium CFD code by accounting for ablation phenomena under an arcjet freestream condition, and the arcjet freestream is determined by using the computer code developed by Sakai and Olejniczak. The integrated computational tool is used to calculate the heating environment for a CFRP ablator tested in a 1 MW arcjet wind tunnel at Institute of Space and Astronautical Science (ISAS) of Japan Aerospace Exploration Agency (JAXA). Obtained results are compared with those calculated by the SCMA code and with the existing experimental data.

In our previous work [5], the thermal conduction and the motion of pyrolysis gas within the ablator was calculated in 2-D space using the SCMA2 code. The boundary condition at an ablating surface was determined by a surface mass and energy balance [9], while an adiabatic wall was assumed at the sidewall of the ablator. A more detailed approach will be made in the present work because the theoretical estimate of the arcjet freestream properties becomes possible, and because the thermochemical state of the flow in the sidewall region can be predicted. In the present analysis, the catalytic effect of an ablating surface on the thermal response of the ablator is examined: different catalytic models are tested to seek a better modeling of the boundary condition at an ablating surface because the surface catalysis of the ablating surface is unknown. Because the surface over the ablating material is believed to be rough, the effect of surface roughness of ablator is examined in the present work.

In this analysis, we omit the momentum equations for pyrolysis gas in the SCMA2 code because the calculation showed unstable when the momentum equations are included. The exact cause of the reason for the instability remains uncertain. To calculate the injection rate of the pyrolysis gas at the surface, the method employed in [10] is used, in which 1-D quasi-steady state is assumed for the motion of the pyrolysis gas. For the heating environment analyzed in the present study, the assumption is believed to be valid because the thickness of a char layer would be thinner enough than that of the test piece. The effect of pyrolysis gas motion inside ablator will be studied in the future.

II. Arcjet Wind Tunnel Operating Condition

The schematic diagram of the 1 MW segmented-constrictor-type arcjet wind tunnel facility in ISAS of JAXA is given in Fig. 1. The facility consists mainly of the upstream electrode chamber (anode),

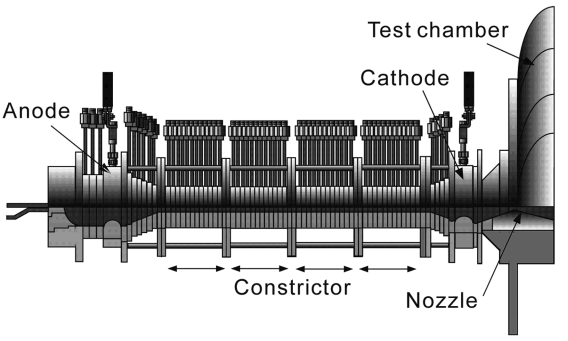

Fig. 1 Schematic of 1 MW arcjet wind tunnel facility installed in ISAS of JAXA.

Table 1 Arcjet operational parameters and flow properties for the operating conditions

Arcjet operational parameters			
Electric current, A		400	
Mass flow rate, kg/s		0.013	
Arcjet freestream properties			
		Calculation	Measurement
Density, kg/m^2		2.122×10^{-4}	——
Velocity, m/s		4956	——
Translational–rotational temperature, K		562.0	——
Vibronic temperature, K		3377.0	——
Mass fraction	N	0.24688	——
	O	0.23286	——
	N_2	0.52014	——
	O_2	0.00001	——
	NO	0.00011	——
Total enthalpy, MJ/kg		25.2	22.7
Mass-averaged enthalpy, MJ/kg		17.4	15 ± 10%
Heat flux, MW/m^2		3.9 (fully catalytic) 1.8 (noncatalytic)	3
Pitot pressure, atm		0.050	0.055

the constrictor, the downstream electrode chamber (cathode), and a converging–diverging nozzle. Air is introduced from the constrictor wall, and is heated by electrical discharge through the constrictor. The hot gas is then expanded through the converging–diverging nozzle into a test chamber. The facility has a constrictor diameter of 2.54 cm. The arc-heater length between electrodes is 75 cm. A conical nozzle was used for the operation analyzed in the present work. The nozzle had a cone half-angle of 10 deg and an exit diameter of 2.5 cm.

In [11,12], the arcjet wind tunnel facility was operated for a wide range of operating conditions to evaluate the operational characteristics of the facility. The operating conditions were controlled by arc current and mass flow rate. Arc-heater operational parameters of arc voltage, heater thermal efficiency, chamber pressure, and mass-averaged enthalpy were measured to evaluate the performance of the arc heater. The mass-averaged enthalpy values were determined by using an energy balance method. Heat flux and impact pressure measurements were done at several axial positions in the test chamber of the tunnel to diagnose the arcjet freestream properties. The heat flux measurements were made using a Gardon gauge.

In our previous work, temperature and pyrolysis gas pressure inside ablative test pieces were measured [13] under one operating condition: 400 A and 0.013 kg/s. The measurement was made at 130 mm from nozzle exit. The measured values of arc-heater operational parameters, heat flux, and impact pressure values are summarized in Table 1. In the table, calculated values are also given. The accuracy of the calculated values will be discussed later.

III. Numerical Methods

Three computational blocks are built to analyze the thermal response of an ablator test piece in an arcjet wind tunnel: 1) simulation of the entire flowfield in an arcjet wind tunnel facility from an upstream end of an upstream electrode chamber to a test section, 2) simulation of thermochemical nonequilibrium shock layer flowfield over an ablator test piece, and 3) simulation of thermal decomposition within the ablator test piece.

A. Arcjet Freestream Calculation

Two subblocks are further built to calculate the flowfield in the 1 MW arcjet wind tunnel facility: one subblock represents the arc-heater section from the upstream electrode chamber to the nozzle throat and another represents the nozzle section downstream of the nozzle throat. In the arc-heater section, the flow is solved using the ARCFLO3 code [6,7]. The nozzle section is simulated by a thermochemical nonequilibrium code [8].

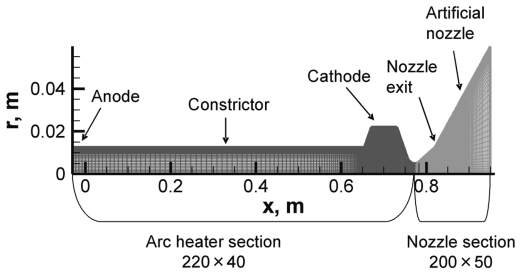

Fig. 2 Computational mesh for 1 MW arcjet wind tunnel facility installed in ISAS of JAXA.

The ARCFLO3 code solves an axisymmetric viscous flow in the arc-heater region from the anode chamber to the nozzle throat. Thermochemical equilibrium is assumed in the flowfield because pressure is typically larger than 1 atm. An air model is used as the test gas which consists of 11 chemical species (N, O, N_2, O_2, NO, N^+, O^+, N_2^+, O_2^+, NO^+, and e−). Mass, momentum, and total energy conservation equations are discretized using a finite volume method. Joule heating and radiative source terms are included in the right-hand side of the energy equations. Solutions are obtained by numerically integrating the equations in time to steady state by using mass flow rate and electrical current as the code input.

In the expanding flow region beyond the throat, the axisymmetric viscous flow is assumed to be in thermochemical nonequilibrium. The air model has five chemical species (N, O, N_2, O_2, and NO). Because the total mass fraction of the ionized species in the throat region is less than 0.001, their contribution is negligible for the present purpose of the calculation. Mass, momentum, vibronic energy, and total energy conservation equations are discretized using a finite volume method. A finite-rate chemical reaction and vibrational relaxation source terms are included in the right-hand side of the mass and vibronic energy equations, respectively. Solutions are obtained by integrating the equations in time. It should be noted that the inlet boundary condition at the entrance of the nozzle is given by the ARCFLO3 solutions at the throat.

Figure 2 shows the computational grid for the 1 MW arcjet wind tunnel. The number of 220×40 grid points is used for the arc-heater region, and that of 200×50 for the nozzle region. As is shown in Fig. 2, an equivalent nozzle extends past the physical exit location to calculate the flow properties at the axial location of the testing of the ablator. The half-angle of the equivalent nozzle is determined to duplicate the measured pitot pressure value [8].

B. Shock Layer Flowfield Analysis

The thermochemical nonequilibrium CFD code [4] is used for the computation of an ablating shock layer flowfield. The governing equations are the Navier–Stokes equations for axisymmetric flowfield, consisting of species mass, momentum, total energy, and vibronic energy conservation equations. The equations are discretized by the cell-centered finite volume scheme using AUSM-DV numerical flux [14] and MUSCL approach for attaining higher-order spatial accuracy. Solutions are obtained by integrating the equations in time to steady state using the LU-SGS algorithm.

For high temperature airflow, we employ the following 11 chemical species: N, O, N_2, O_2, NO, N^+, O^+, N_2^+, O_2^+, NO^+, and e^-. Moreover, we consider the following ten species as the ablation product gas: C, C_2, CN, CO, C_3, C^+, H, H_2, H^+, and C_2H. The total number of chemical species used in the present analysis is 21.

Park's two-temperature model is employed to determine the thermochemical nonequilibrium states. The vibronic energy conservation equation accounts for 1) vibrational energy excitation of molecules through collisions between heavy particles, 2) elastic energy transfer between electrons and heavy particles, 3) gains or losses of energy by electron impact ionization, and 4) gains or losses of vibronic energy of heavy particles in chemical reactions [15]. Vibrational relaxation parameters, such as a vibrational relaxation time, are taken from [16,17]. The relaxation time is accounted for

Park's limiting cross section at high temperature. The values of reaction rate coefficients are taken from [16,18].

In the present study, we consider the following four types of chemical reactions that occur at the ablator surface: 1) oxidation by atomic oxygen that produces CO, 2) nitridation by atomic nitrogen that produces CN, 3) sublimation that produces C_3, and 4) catalytic recombination of nitrogen and oxygen. The surface reaction velocity is given by kinetic theory as

$$k_i = \frac{\alpha_i}{4}\sqrt{\frac{8\bar{R}T_w}{\pi M_s}} \tag{1}$$

Thus, mass fluxes of CO and CN due to oxidation and nitridation reactions are given by

$$J_{\mathrm{CO}} = \frac{M_{\mathrm{CO}}}{M_{\mathrm{O}}}\rho_{\mathrm{O}}\frac{\alpha_{\mathrm{oxi}}}{4}\sqrt{\frac{8\bar{R}T_w}{\pi M_{\mathrm{O}}}} \tag{2}$$

$$J_{\mathrm{CN}} = \frac{M_{\mathrm{CN}}}{M_{\mathrm{N}}}\rho_{\mathrm{O}}\frac{\alpha_{\mathrm{nit}}}{4}\sqrt{\frac{8\bar{R}T_w}{\pi M_{\mathrm{N}}}} \tag{3}$$

The reaction probability of oxidation reaction is taken from [15], and is expressed as

$$\alpha_{\mathrm{oxi}} = 063\exp\left(-\frac{1160.0}{T_w}\right) \tag{4}$$

As for the probability of nitridation reaction, the value has been experimentally determined by Park as follows [19]:

$$\alpha_{\mathrm{nit}} = 0.3 \tag{5}$$

Mass flux of C_3 due to sublimation is given by Hertz–Knudsen–Langmuir equation [20] as

$$J_{\mathrm{C_3}} = \frac{\alpha_{\mathrm{sub}}\max(0, p_{e,\mathrm{C_3}} - p_{\mathrm{C_3}})}{\sqrt{2\pi\bar{R}T_w/M_{\mathrm{C_3}}}} \tag{6}$$

Equilibrium vapor pressure $p_{e,\mathrm{C_3}}$ and the reaction probability are given, respectively, by

$$p_{e,\mathrm{C_3}} = 9100.0\times 10^{15}T_w^{-1.5}\exp\left(-\frac{97,597.0}{T_w}\right)\times 133.322\ \mathrm{Pa} \tag{7}$$

$$\alpha_{\mathrm{sub}} = 0.023 \tag{8}$$

The catalytic recombination process at the ablating surface is represented by either noncatalytic or fully catalytic condition. Each of the catalytic efficiencies is given by the following relation for N and O, respectively:

Noncatalytic wall case:

$$\alpha_{\mathrm{cat_N}} = 0 \tag{9}$$

$$\alpha_{\mathrm{cat_O}} = 0 \tag{10}$$

Fully catalytic wall case:

$$\alpha_{\mathrm{cat_N}} = 1 - \alpha_{\mathrm{nit}} \tag{11}$$

$$\alpha_{\mathrm{cat_O}} = 1 - \alpha_{\mathrm{oxi}} \tag{12}$$

By imposing Eqs. (11) and (12), the sum of the mass flux of oxygen and nitrogen that consumed by oxidation, nitridation, and catalytic recombination never exceeds the mass flux of atomic oxygen and nitrogen striking the wall. The concentration of the species at the catalytic surface is calculated by dictating that the production rate at the surface balances with the diffusion rate.

The reaction probabilities in Eqs. (4) and (5) were usually measured by using smooth solid carbon materials. However, the surface of ablative material is most likely rough, which has deep crevices. When deep crevices develop, an oxygen (or a nitrogen) atom emerging from the inside of crevices collides several times with another part of the wall inside the crevice before it leaves the crevice. As a result, the process occurring over the ablating surface with roughness accelerates the oxidation and nitridation. In a limiting case, the reaction probabilities could be taken to be unity as follows [15]:

$$\alpha_{\mathrm{oxi}} = 1 \tag{13}$$

$$\alpha_{\mathrm{nit}} = 1 \tag{14}$$

It should be noted in this case that the catalytic efficiencies for N and O become zero. Therefore, the ablating wall with roughness leads to the noncatalytic one with the oxidation and nitridation reactions enhanced. The effect of the enhanced reaction probabilities on the computed thermal response will be discussed later.

The molecular viscosity for each chemical species is either given by Blottner's model [21] or by a curve fit. The thermal conductivity is given by Eucken's relation [22]. The total viscosity and conductivity are calculated using Wilke's empirical mixing formula [23]. We assume the diffusion coefficient to be constant for all species with a constant Schmit number of 0.5.

C. Thermal Response Analysis

The thermal response of ablative test piece is calculated by the SCMA2 code [5]. The governing equations can be written in integral form as

$$\frac{\partial}{\partial t}\int_\Omega \boldsymbol{Q}\,\mathrm{d}\Omega + \int_S \boldsymbol{F}_j\,\mathrm{d}S = \int_\Omega \boldsymbol{W}\,\mathrm{d}\Omega \tag{15}$$

Components of the conservative variables $\boldsymbol{Q}$, the flux vector $\boldsymbol{F}_j$, and the source term $\boldsymbol{W}$ are given, respectively, as follows:

$$\boldsymbol{Q} = \begin{pmatrix} \rho_r \\ \rho_r e_r + \rho_c e_c \end{pmatrix}, \qquad \boldsymbol{F}_j = \begin{pmatrix} 0 \\ \dot{m}_g e_g - \kappa_j \partial T/\partial x_j \end{pmatrix}$$
$$\boldsymbol{W} = \begin{pmatrix} -R \\ 0 \end{pmatrix} \tag{16}$$

The thermal properties of resin and char are determined separately. The density of solid state ρ_s is thus given by a sum of that for char and resin as

$$\rho_s = \rho_c + \rho_r(\rho_c = \mathrm{const.}) \tag{17}$$

The internal energy for solid state is divided into that of char and resin, and is given by

$$e_c = H_{0c} + \int c_{pc}(T)\,\mathrm{d}T \tag{18}$$

$$e_r = H_{0r} + \int c_{pr}(T)\,\mathrm{d}T \tag{19}$$

As was done in [10], the motion of pyrolysis gas is assumed to be 1-D along the normal direction to ablating surface in general body fitted coordinate system, and the mass flux of pyrolysis gas is calculated using following approximation:

$$\dot{m}_g(\eta_x) = \frac{1}{A}\int_0^{\eta_x} RA\,\mathrm{d}\eta \tag{20}$$

The pyrolysis rate R in Eqs. (16) and (20) is expressed as

$$R = \sum_{k=1}^{N} f_k A_k \exp\left(-\frac{B_k}{T}\right)(\rho_v - \rho_c)\left(\frac{\rho_s - \rho_c}{\rho_v - \rho_c}\right)^{\mu_k} \tag{21}$$

Pyrolysis Eq. (21) was determined by the least-squares method to reproduce the thermograms of the thermogravimetry data obtained in

a different series of experiment. As a results, four component expression, $N = 4$, gave the best-fit curve.

The thermal conduction is assumed to be isotropic. The value of the thermal conductivity is calculated by a weighted sum of that for char and virgin material:

$$\rho_s \kappa_x = \rho_s \kappa_y = (1 - \omega)\rho_c \kappa_c(T) + \omega \rho_v \kappa_v(T) \tag{22}$$

where $\omega = (\rho_s - \rho_c)/(\rho_v - \rho_c)$. Potts showed that the specific heat of graphite was nearly a linear function of temperature ($c_p \approx c_1 T$) for the lower-temperature regime, whereas it was almost constant (c_∞) for very high temperature [24]. Therefore, the specific heat of the solid is given by the following bridging form:

$$c_p = c_\infty [T/\sqrt{T^2 + (c_\infty/c_1)^2}] \tag{23}$$

D. Coupling Method

Ablation is essentially a time-dependent phenomenon. To analyze the thermal response of ablator with a time-dependent manner using the SCMA2 code, the boundary condition must be updated at each time step. The SCMA2 code needs two boundary conditions: pressure and heat flux. Because the time variation of the heat flux and pressure values are not known a priori, one needs to know the heat fluxes and pressure distributions along an ablating surface as a function of time.

The heat flux and pressure distributions at a given time step is determined using a converged solution obtained by a coupled method between the SCMA2 code and the thermochemical nonequilibrium CFD code. An iteration procedure is needed to obtain the converged solution. First, the shock layer flowfield solution over an ablative test piece is calculated without ablation using the CFD code. The calculated heat flux and pressure distributions at the surface are taken to be the initial condition at $t = 0$ s for the SCMA2 code. Next the SCMA2 calculation is carried out until a specified time step is reached. The pyrolysis gas injection rate and wall temperature at the surface are obtained at the time step using the SCMA2 code. A shock layer flowfield calculation is made with ablation using the pyrolysis gas injection rate and wall temperature so obtained, and the values of the heat flux and the pressure along the ablating surface are evaluated. A SCMA2 calculation is made from $t = 0$ s to the specified time step to update the values of the pyrolysis gas injection rate and wall temperature. This procedure is repeated until the heat flux and the pressure distributions are unchanged compared with those at a previous iteration. In the present study, it is found that we need three or four iterations to obtain convergence.

The iteration procedure is needed at each time step to carry out the thermal response calculation of the ablator test piece during arcjet testing. Even though only three or four iterations are needed to obtain convergence in the coupled method, this procedure is very time-consuming. Therefore, one needs to choose several coupling calculation points to reduce the computing time. In the present study, we select eight points at $t = 1, 3, 5, 10, 15, 20, 25$, and 30 s. The heat flux and pressure values in between the selected times are linearly interpolated from two known values.

The pyrolysis gas injection rate at the ablating surface is given by the SCMA2 code as

$$\dot{m}_g(\eta_w) = \frac{1}{A}\int_0^{\eta_w} RA \, \mathrm{d}\eta \tag{24}$$

The chemical composition of pyrolysis gas at the wall surface is calculated by assuming thermochemical equilibrium condition. The net heat flux transferred to the wall surface is composed of the energy transport by convection and radiation, and is given by

$$q_{\text{net}} = \left(\kappa \frac{\partial T}{\partial n}\right) + \left(\kappa_{\text{vib}} \frac{\partial T_{\text{vib}}}{\partial n}\right) + \left(\sum_s \rho D_s \frac{\partial c_s}{\partial n} H_s\right) + q_R - \varepsilon \sigma T_w^4 \tag{25}$$

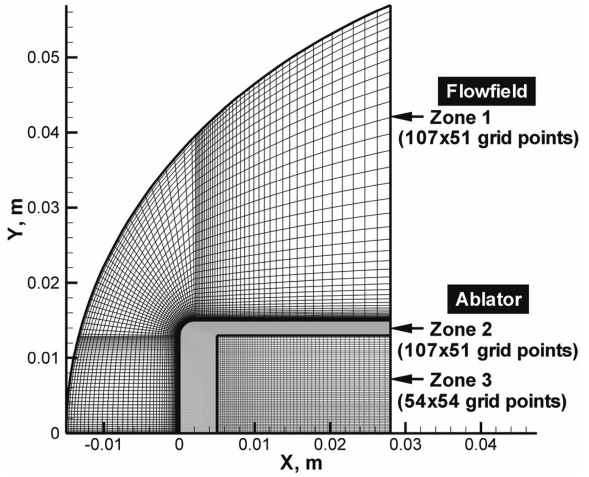

Fig. 3 Computational meshes for shock layer calculation and thermal response analysis.

Because the shock layer radiation q_R is negligibly small, it is not included in the present study.

As to the surface recession, the SCMA2 code itself does not take account of surface recession explicitly. It is implicitly accounted in the code by changing the position of the outer wall surface and redraws the numerical mesh inside the ablator. The mass loss rate r_c and the amount of recession S in the normal direction to the surface are obtained from the CFD solution as

$$r_c = \frac{(M_C/M_{CO})J_{CO} + (M_C/M_{CN})J_{CN} + (M_C/M_{C_3})J_{C_3}}{\rho_c} \tag{26}$$

$$S = \int r_c \, \mathrm{d}t \tag{27}$$

In the flowfield calculation, the effect of recession is included by redrawing the mesh at each calculation point. A typical example of computational meshes for both flowfield and ablative test piece are shown in Fig. 3. The zone 1 with 107×51 grid points is used for the flowfield calculation. Note that the computational domain for the ablator is divided into two zones. The zone 2 has 107×51, and the zone 3 has 54×54 grid points. The grid points in the zone 3 remain fixed in the course of simulation, and those in the zone 2 are compressed to account for shape change.

In the present study, the thermochemical nonequilibrium CFD code is parallelized with OpenMP directives. All the flowfield calculations are performed using the CFD code on four processors of Fujitsu PRIMEPOWER HPC2500, which is the central machine of Numerical Simulator III system in JAXA. Approximately 60,000 iteration steps are needed to drop the L2-norm of the residual six orders of magnitude, requiring about 8 h of CPU time. The CPU times for the thermal response analysis vary depending on the time specified for the coupling calculation point and the time-step size, and are the order of a few CPU hours or less. The total CPU time was 336 h (two weeks) for the typical computational meshes used in the present study.

E. Initial Heat Flux Distribution at Surface

A flowfield solution over the ablative test piece is calculated without ablation under the arcjet operating condition. The catalytic efficiency on the wall surface of the test piece is taken to be the fully or the noncatalytic condition for this case. In Fig. 4, the calculated wall heat fluxes are plotted against the distance along the wall surface. From the figure, one can see that the calculated heat flux value increases up to the corner of the test piece along the frontal surface, and decreases gradually on the side surface. On the frontal surface, the calculated heat fluxes using the fully catalytic condition is higher by a factor of 2 compared to the ones using the noncatalytic condition. Because the true value of the surface catalytic efficiency at

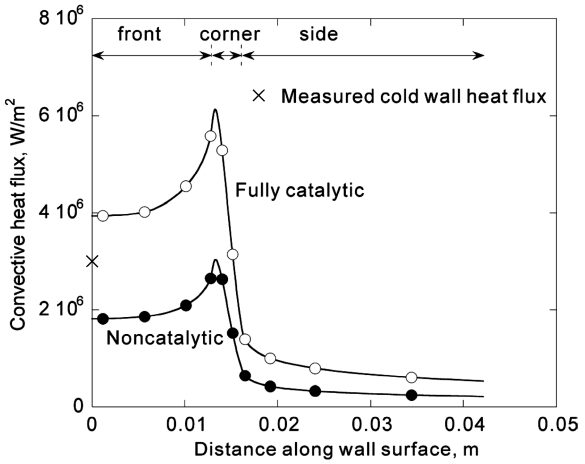

Fig. 4 Heat flux along wall surface without ablation.

the ablating surface is unknown, thermal response calculations are made using these two limited catalytic conditions at the ablating surface.

The value of the cold wall heat flux measured at the stagnation point is also given in Fig. 4. One-dimensional SCMA calculation will be made later for the purpose of comparison. In the SCMA calculation, the cold wall heat flux value is used as the boundary condition.

F. Calculated Arcjet Freestream Properties

Calculated flow properties in the arcjet freestream are given in Table 1. The calculated pitot pressure and heat flux values at the stagnation point are compared with the measured values. The calculated pitot pressure value is in good agreement with the measurement. This is because the settling chamber pressure calculated by using ARCFLO3 agrees with the measurement. The measured heat flux value is 25% lower than the calculated one with the fully catalytic wall, and is higher by about 50% than the one with the noncatalytic wall. The cause of the difference of the heat flux between calculation and measurement may stem from two major uncertainties: the catalytic efficiency of the heat flux gauge and the total enthalpy of the calculated arcjet flow.

The heat flux was measured using the Gardon gauge, and the catalytic efficiency of the gauge is usually assumed to be fully catalytic. However, the catalytic efficiency could be reduced when it is in a dissociated flow. The arcjet freestream contains atomic nitrogen and oxygen, as was shown in Table 1. Therefore, the convective heat transfer rate could be decreased to some extent depending on the degree of the atomic recombination. In the experiments, the true value of the catalytic efficiency was unknown. The total enthalpy at the centerline of the arcjet flow was deduced theoretically using the method given by Zoby [25]. The enthalpy value deduced was 22.7 MJ/kg. This value was lower than the calculated centerline enthalpy (25.2 MJ/kg) by about 10%. However, because the measured heat flux value is sensitive to the possible catalytic efficiency on the Gardon gauge, the enthalpy value deduced from the theoretical method can be affected also. Because there is no other experimental information for the total enthalpy, it is difficult to access the accuracy of the calculated total enthalpy value in the present study. An assessment of the arcjet freestream properties such as total enthalpy, concentration of species or velocity, etc., by using the present calculation method is left for the future.

IV. Results and Discussion

A. Outline of Thermal Response of Ablative Test Piece Under an Arcjet Flow Condition

A coupled thermal response calculation inside an ablative test piece is carried out for the arcjet operating condition: 400 A and 0.013 kg/s. The thermal response calculation continues up to $t = 50$ s to see the effect of a so-called heat soaking phenomenon, although the ablative test piece was removed after the exposure time of 30 s. For the present calculations, two mesh systems are used: a standard mesh and a fine mesh as is given in Table 2. Calculations show that there is little difference of the temperature distribution inside the ablator test piece between the two mesh systems, as will be shown later. The calculated results presented next are those using the standard mesh system.

Table 2 Number of grid points for each zone

	Standard	Fine
Zone 1	107×51	217×101
Zone 2	107×51	217×101
Zone 3	54×54	109×109

Calculated temperature and density distributions inside the test piece are shown in Figs. 5a–5d for the case of noncatalytic wall. Figures 5a–5d correspond to the time period at $t = 0$, 10, 30, and 50 s, respectively, A similar trend is seen for the case of the fully catalytic wall condition, and the results are omitted here. One can see from Fig. 5b that the phenolic resin begins to decompose when temperature within the ablator begins to increase, and a char layer is left behind the pyrolysis zone. Figures 5c and 5d represent the results after the exposure time has elapsed. From these figures, the temperature inside the test piece increases due to heat soak, while the surface temperature decreases. As a result, the density in the pyrolysis zone (designated in green and yellow shown in Fig. 5d) continues to decrease.

One can also see from Figs. 5a–5c that the surface of the ablative test piece is receding due to the wall reactions occurred at the ablating surface. By comparing the calculated results between Figs. 5a and 5c, the difference of the surface shape between before and after heating is clearly recognized. However, the calculated result could not be directly compared with the test piece, because we could not measure the amount of the recession of the actual test piece due to the thermal expansion of the test piece.

B. Distributions of Temperature and Recession Along Wall Surface

Figure 6 shows the surface temperature distributions along the wall surface at $t = 1$, 30, and 50 s from the onset of heating, respectively. The results are presented for the fully and noncatalytic and rough surface cases, respectively. The result for the rough surface case will be discussed later. At $t = 1$ s, the surface temperatures at the corner of the test piece for both cases are about 20% larger than those at the stagnation region. This difference is caused due to the moderate heating rate around the corner of the test piece compared with the stagnation region. As contrary to expectation, the surface temperature profile along the front wall surface becomes almost uniform at $t = 30$ s. This uniform surface temperature distribution is a consequence that the surface contour of the ablative test piece changes, and that it becomes rather smooth during the 30 s of exposure time, as shown in Fig. 5. At $t = 50$ s, the temperatures along the ablator surface for both cases decrease due to the radiative cooling. As shown in Fig. 6, the calculated temperatures for the fully catalytic case are higher than those for the noncatalytic case. This difference is due to the fact that the heat fluxes obtained by the fully catalytic wall condition are higher than those by the noncatalytic condition, as expected.

The calculated surface contours of the ablative test piece at $t = 30$ s are shown in Fig. 7 for the cases of the fully and noncatalytic and rough surface, and uncoupled with flowfield cases, respectively. The results for the rough surface and uncoupled case will be discussed later. The surface receded approximately by 1 mm at the stagnation point after the 30 s of exposure time for the noncatalytic case. Note that the amount of recession for the noncatalytic case is larger than that for the fully catalytic case, though the surface temperature for the noncatalytic case is lower than that for the fully catalytic case.

To understand the observed trend for the calculated shape of the test piece for the fully and noncatalytic wall conditions shown in Fig. 7, calculations are carried out independently by imposing a

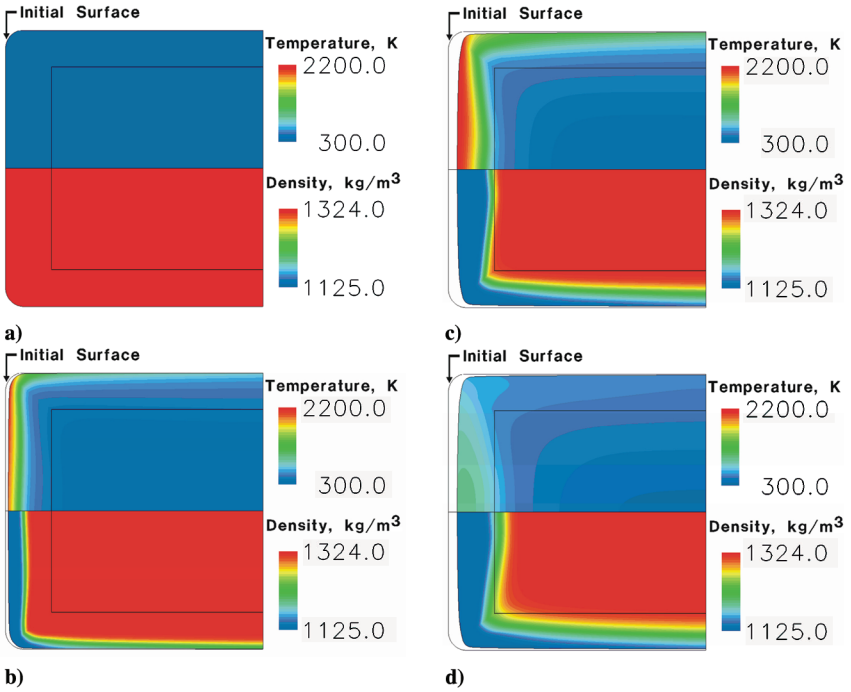

Fig. 5 Thermal response of ablative test piece under arcjet flow condition. Calculated temperature contour (top) and density contour (bottom) are shown: a) $t = 0$ s from onset of heating, b) $t = 10$ s from onset of heating, c) $t = 30$ s from onset of heating, d) $t = 50$ s from onset of heating.

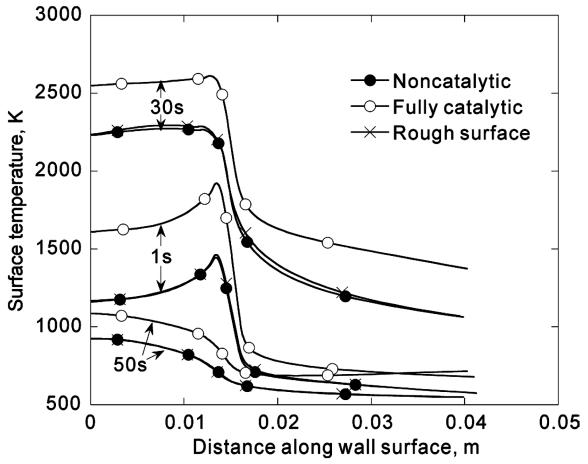

Fig. 6 Surface temperature profiles along wall surface at $t = 1, 30$, and 50 s from onset of heating.

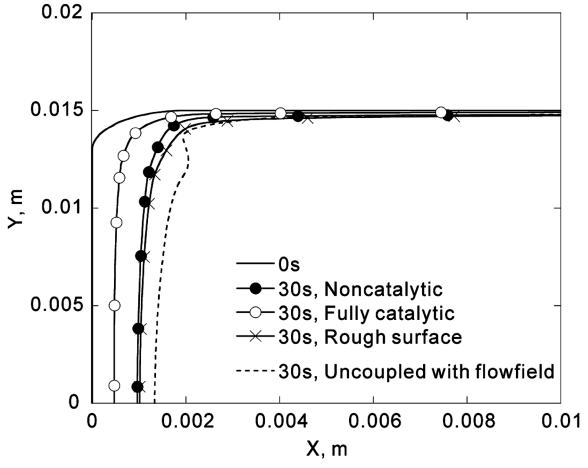

Fig. 7 Calculated surface contours at $t = 30$ s from onset of heating.

constant wall temperature ranging from 1500 to 3500 K. The pyrolysis gas injection is not accounted for in these calculations because the effect of wall temperature on the amount of the mass flux produced by the chemical reactions occurring at ablating surface is concerned.

Computed mass flux values at the stagnation point are plotted against the wall temperature in Fig. 8. Note that the amount of the calculated mass flux compares to that of the recession shown in Fig. 7. For the purpose of comparison, the mass flux values using the correlation formula for graphite ablation proposed by Metzger et al. [26] are given in the same figure. According to Metzger et al., the mass flux values are divided into three regimes: reaction-controlled, diffusion-controlled, and sublimation. The three regimes are also given in the figure. Based on these divided regimes, it is found for both of the fully and noncatalytic cases that the calculated mass fluxes in the wall temperatures from 1500 to 3000 K represent the diffusion-controlled regime, and that the mass fluxes in the wall temperatures over 3000 K show the sublimation regime. One can see that the mass flux values calculated by the fully catalytic condition are closer to those given by using the Metzger et al. formula in the diffusion-controlled regime.

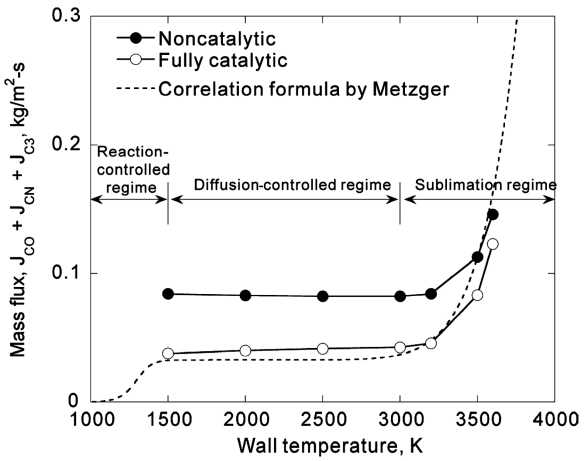

Fig. 8 Variations of mass flux due to wall reactions against wall temperature.

In the diffusion-controlled regime, the mass flux calculated by using the fully catalytic condition is lower than that calculated by using the noncatalytic condition. This trend is explained as follows: The amount of the mass flux in the diffusion-controlled regime is governed by the amount of atomic oxygen and nitrogen striking the wall surface, as was shown in Eqs. (2) and (3). These atomic species recombine in the boundary layer when the fully catalytic wall condition is imposed, whereas no recombination reaction occurs for the noncatalytic wall condition. Therefore, the amount of these atomic species striking the wall surface becomes lower for the case of the fully catalytic wall than for that of the noncatalytic wall. On the other hand, in the sublimation regime, the difference of the mass flux values between the fully and the noncatalytic cases are relatively small. This is because the sublimation reaction is dictated mostly by the wall temperature, and is not affected by the amount of the atomic species, as was shown in Eq. (6).

In Figs. 6 and 7, the calculated results using the present rough surface case are compared with those for the fully and noncatalytic cases. Note that for the rough surface case, the wall is noncatalytic for atomic nitrogen and oxygen recombination reactions. From Fig. 6, although the surface reactions for oxidation and nitridation are enhanced, as explained in the numerical method [see Eqs. (13) and (14), respectively], the only discernible difference is seen in the calculated surface temperature data between the noncatalytic case and the roughness case. Figure 7 shows that the calculated amount of the recession at $t = 30$ s for the rough surface case is only slightly larger than that for the noncatalytic case. These results suggest that the amount of atomic oxygen and nitrogen reaching to the ablating surface for the roughness case is nearly the same as that for the noncatalytic case. As is given by Eqs. (2) and (3), the mass fluxes are determined by surface temperature and atomic species density. Because the recession and the surface temperature are nearly the same between the two cases, the atomic species densities should be in a same level.

To quantify the effect of the roughness model to the thermal response of the ablator, more work will be needed. The amount of the atomic oxygen and nitrogen species striking the ablating wall will be changed by changing an arcjet operating condition. Mass flow rate and electrical current were relatively small in the arcjet environment analyzed in the present study. Increasing these two operating parameters increases the stagnation point pressure and the dissociation level of molecular nitrogen in the test section. Pyrolysis gas injection rate will also be changed by changing the arcjet freestream condition. In addition, if the exposure time span that the ablator is put into an arcjet flow lengthens more, the surface temperature could be increased and could affect the mass flux, as was indicated from the results in Fig. 8. To examine these effects in an arcjet environment with a coupled manner, the established approach in the present study is believed to be most essential.

Uncoupled calculation with shock layer flowfield is also carried out for the purpose of comparison. In this case, the initial heat flux profile at $t = 0$ s was used for the boundary condition of the SCMA2 code for the 30 s of duration time. The resulting surface contour is also shown as dotted line in Fig. 7. One can see that the surface contour becomes indented near the corner of the test piece. This trend is qualitatively different from the final test piece after testing. It should be noted that the result obtained in the present study is also seen in the work by Chen and Milos [10]. It is suggested from the results that the accurate prediction of heating environment with ablation is only available when the coupled analysis of flowfield and thermal response of ablator is accomplished.

C. Properties at Stagnation Point

In this subsection, the results of the present coupled analysis for both of the fully and noncatalytic cases are shown especially focusing on the stagnation point. These results are compared with the 1-D SCMA calculations along the centerline of the test piece and with measured temperature data [13]. For the SCMA calculations, the mass and energy balance at the ablating surface is determined using the procedure developed by Potts [9], not given by the present coupled approach. The validation study of the SCMA code against the present experimental data can be found in [13].

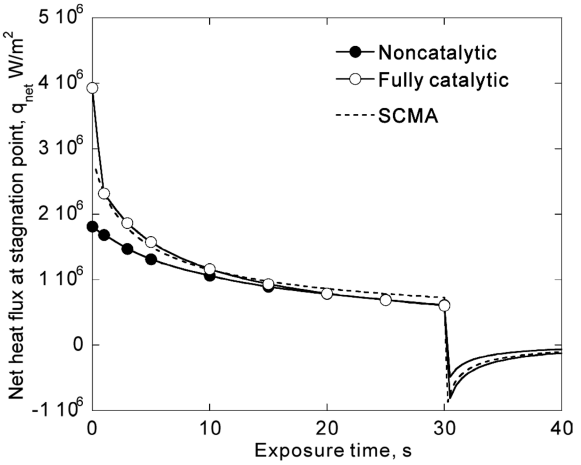

Fig. 9 Net heat flux variation at the stagnation point.

Figure 9 shows the time history of the net heat flux transferred to the wall surface at the stagnation point. The net heat flux q_{net} is defined in Eq. (25). From the figure, the net heat fluxes for both of the fully and noncatalytic cases decrease from the onset of heating because the radiative cooling and the convective blockage effect become stronger as the pyrolysis gas injection rate increases. At $t = 0$ s, the difference of the net heat fluxes between the fully and noncatalytic cases is a factor of 2 as was seen in Fig. 4. After $t = 0$ s, the calculated q_{net} with the fully catalytic wall approaches to the one with the noncatalytic wall. This trend is because the reaction probability of oxidation α_{oxi} given in Eq. (4) becomes larger as the wall temperature increases. As a result, the catalytic efficiency of atomic oxygen α_{cat_O} decreases as can be seen in Eq. (12). After $t = 30$ s, the radiative heat flux is the only component of the net heat flux. The q_{net} value calculated with the fully catalytic wall is higher than that with the noncatalytic one due to the fact that the surface temperature calculated by the fully catalytic wall condition is larger than that calculated by the noncatalytic wall. The temperature of the test piece is explained in a next subsection. The SCMA2 calculation gives a good agreement with the data calculated by using the SCMA code.

The surface temperature variation at the stagnation point is plotted against time in Fig. 10. The results are presented for the SCMA2 calculations using the two catalytic conditions, the SCMA calculation, and the measurement [13]. For the SCMA2 calculations, the results are shown for the cases with and without nitridation reaction. In the measurement, the surface temperature of the test piece was measured by a one-color optical pyrometer. The experimental error was estimated to be less than 5%. As shown in the

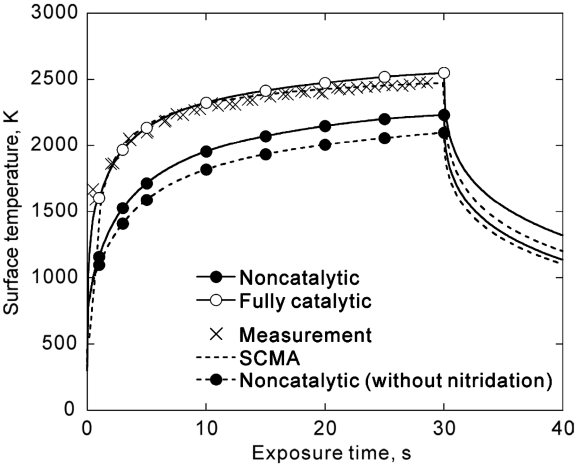

Fig. 10 Comparison of calculated surface temperature variations with experimental data.

figure, the surface temperature increases rapidly from the onset of heating. One can see that the temperature calculated for the fully catalytic case is larger than the one for the noncatalytic case. This trend is because the net heat flux for the fully catalytic case is higher during the 30 s of exposure time than that for the noncatalytic case. The present calculation overestimates the measured temperature for the case of the fully catalytic condition, and underestimates for the noncatalytic case. This result implies that the measured temperature profile can be reproduced by the present coupled analysis if we use an assumed catalytic efficiency on the wall surface. Empirically, even when the small catalytic efficiency value ($\sim$0.1) is used in the calculation, the calculated temperature profiles are nearly identical to those calculated with the fully catalytic wall. Based on the empirical result, it is expected that calculation with a small catalytic efficiency can predict the measured surface temperature for the heating environment analyzed in this study.

From the comparison between the cases with and without nitridation reaction for the noncatalytic case, one can see that the temperature for the case with nitridation reaction becomes about 100 K larger than that for the case without nitridation reaction for the 30 s of exposure time. The calculated result approaches to the measured temperature. This large increase in temperature is explained as follows: The heat release by nitridation is equal to 0.35 eV:

$$\mathrm{N} + \mathrm{C}(s) \rightarrow \mathrm{CN} + 0.35\ \mathrm{eV} \tag{28}$$

This energy will not be so high that the surface temperature was increased as much as 100 K. But, the CN molecules produced by nitridation react with N to produce $N_2 + C$ in the gas phase,

$$\mathrm{CN} + \mathrm{N} \rightarrow \mathrm{N}_2 + \mathrm{C} + 2.04\ \mathrm{eV} \tag{29}$$

This reaction is also exothermic. Though not shown here, the mass fraction of N_2 is about 0.45 near the wall surface when the surface nitridation reaction is included. Note that the net heat generated by the two reactions is nearly equal to that of oxidation reaction,

$$\mathrm{O} + \mathrm{C}(s) \rightarrow \mathrm{CO} + 3.74\ \mathrm{eV} \tag{30}$$

The time history of surface recession at the stagnation point for the arcjet testing is shown in Fig. 11 for the cases of the SCMA2 calculations with the two catalytic conditions and the SCMA calculation. For the SCMA2 calculations, the result for the case without the nitridation reaction is shown in the same figure. One can see that the wall surface recedes almost linearly with time. This linear recession is explained as follows: As shown in Fig. 10, the calculated wall temperature for the SCMA2 calculations is found to be within a range between 1500 and 2500 K. At such temperatures, the mass loss rate is almost constant, as shown in Fig. 8. As a result, the wall surface recedes linearly with time. As shown in this figure, the recession

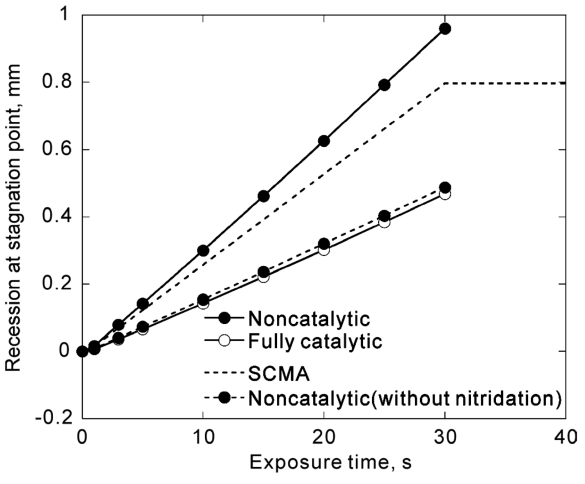

Fig. 11 Time history of surface recession at the stagnation point.

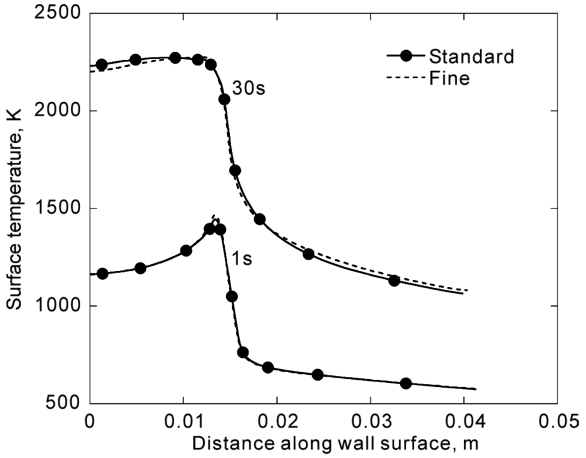

Fig. 12 Surface temperature distributions at $t = 1$ and 30 s for two meshes.

calculated by the noncatalytic condition is closer to the one given by the SCMA code.

From the figure, the amount of the recession calculated by the noncatalytic condition is larger than that calculated by the fully catalytic condition. This trend is due to the fact that the amount of atomic oxygen and nitrogen striking the wall surface becomes lower for the case of the fully catalytic wall than for that of the noncatalytic wall, as was mentioned earlier. The recession obtained by the SCMA calculation is in between the two SCMA2 calculations. This trend is the same as the one seen in the surface temperature variation, as was shown in Fig. 10. On the other hand, the recession calculated without nitridation reaction becomes smaller than that obtained by the SCMA code. This result indicates that one can fail to predict the amount of recession if the nitridation reaction is not accounted for. More experimental data will be needed to confirm the effect of the nitridation.

D. Grid Convergence Study

Grid convergence is examined by comparing results obtained by using the two mesh systems: standard and fine meshes. The number of grid points used in this study is summarized in Table 2. Obtained surface temperature distributions for the case of noncatalytic wall at $t = 1$ and 30 s are shown in Fig. 12. For the fully catalytic case, similar trend is seen and the results are omitted here. One can see that there are no significant differences between the results obtained by two meshes at $t = 1$ s. At $t = 30$ s from the onset of heating, the temperature calculated using the fine mesh becomes slightly lower than that calculated using the standard mesh at the front of the test piece, but the difference is less than 1.5% at the stagnation point. Figure 13 shows the calculated surface contours of the ablative test

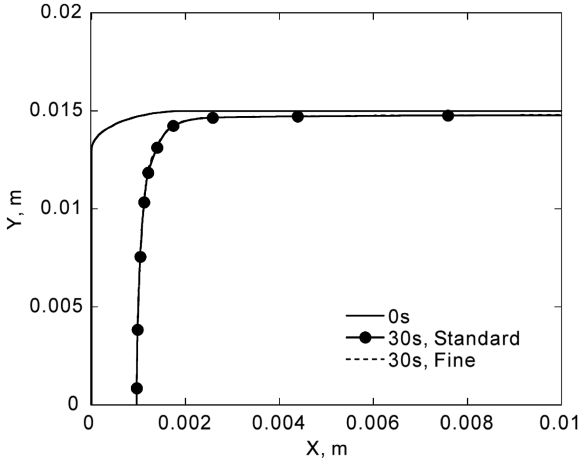

Fig. 13 Comparison of surface contours obtained by using two meshes.

piece at $t = 30$ s. As can be seen, solution calculated by using the fine mesh duplicate well with that calculated by using the standard mesh, indicating that the grid converged solution is obtained.

V. Conclusions

An integrated computational method is developed to calculate thermal response of ablator that is put into arcjet flow. The method can be used to study the thermal response inside an ablator accounting for the ablating shock layer flowfield. The ablating shock layer flowfield is calculated with the arcjet freestream predicted by accounting for the heating and relaxing process occurred in the arcjet wind tunnel entirely theoretically. To analyze the ablating surface more detail, the nitridation reaction and the surface roughness effect are implemented into the thermal response code.

Using the integrated computational tool, the heating test of ablator test piece conducted in the 1 MW arcjet wind tunnel at ISAS of JAXA is analyzed for one operating condition. The shape of the material surface calculated by the present coupled approach is qualitatively consistent with the one obtained in the arcjet testing. Note that one can fail to predict the amount of the recession when the thermal response calculation is made without accounting for the thermochemical state of the ablating layer. The difference between the two catalytic conditions at the ablating surface analyzed in the present study is relatively large. Especially, the amount of recession for the fully catalytic case becomes smaller than that for the noncatalytic case, though the surface temperature for the fully catalytic case is higher than that for the noncatalytic case. The effect of the nitridation reaction on the computed thermal characteristics of the ablator is large, but the result is not so changed with and without surface roughness for the present operating condition. Further investigation will be needed to quantify the effect of the surface roughness by changing the arcjet operating condition.

Acknowledgment

This work was partly supported by the Grant-in-Aid for Young Scientists (B) (No. 18760613) from the Ministry of Education, Culture, Sports, Science and Technology in Japan.

References

[1] Working Group of Asteroid Sample Return Mission, "A Program of Exploring an Asteroid (MUSES-C), The Proposal," Institute of Space and Astronautical Science, Kanagawa, Japan, March 1995.

[2] Ahn, H.-K., Park, C., and Sawada, K., "Response of Heatshield Material at Stagnation Point of Pioneer-Venus Probe," *Journal of Thermophysics and Heat Transfer*, Vol. 16, No. 3, 2002, pp. 432–439.

[3] Moyer, C. B., and Rindal, R. A., "An Analysis of the Coupled Chemically Reacting Boundary Layer and Charring Ablator, Part 2, Finite Difference Solution for the In-Depth Response of Charring Materials Considering Surface Chemical and Energy Balances," NASA CR-1061, June 1968.

[4] Suzuki, T., Furudate, M., and Sawada, K., "Unified Calculation of Hypersonic Flowfield for a Reentry Vehicle," *Journal of Thermophysics and Heat Transfer*, Vol. 16, No. 1, 2002, pp. 94–100.

[5] Suzuki, T., Sawada, K., Yamada, T., and Inatani, Y., "Thermal Response of Ablative Test Piece in Arc-Heated Wind Tunnel," AIAA Paper 2004-0341, Jan. 2004.

[6] Sakai, T., and Olejniczak, J., "Improvements in a Navier-Stokes Code for Arc Heater Flows," AIAA Paper 2003-3782, June 2003.

[7] Sakai, T., "Computational Simulation of High Enthalpy Arc Heater Flows," *Journal of Thermophysics and Heat Transfer* (to be published).

[8] Sakai, T., Suzuki, T., Fujita, K., and Ito, T., "Calculation of High Enthalpy Aerothermal Environment in an Arcjet Wind Tunnel," *Journal of Thermophysics and Heat Transfer* (to be published).

[9] Potts, R. L., "Hybrid Integral/Quasi-Steady Solution of Charring Ablation," AIAA Paper 90-1677, June 1990.

[10] Chen, Y.-K., and Milos, F. S., "Two-Dimensional Implicit Thermal Response and Ablation Program for Charring Materials," *Journal of Spacecraft and Rockets*, Vol. 38, No. 4, 2001, pp. 473–381.

[11] Hinada, M., Inatani, Y., Yamada, T., and Hiraki, K., "An Arc-Heated High Enthalpy Test Facility for Thermal Protection Studies," Institute of Space and Astronautical Science, Rept. 664, Sagamihara, Japan, March 1996.

[12] Yamada, T., and Inatani, Y., "Arc Heating Facility and Test Technique for Planetary Entry Missions," Institute of Space and Astronautical Science, Rept. SP17, Sagamihara, Japan, March 2003.

[13] Suzuki, T., Sawada, K., Yamada, T., and Inatani, Y., "Experimental and Numerical Study of Pyrolysis Gas Pressure in Ablating Test Piece," *Journal of Thermophysics and Heat Transfer*, Vol. 19, No. 3, 2005, pp. 266–272.

[14] Wada, Y., and Liu, M. S., "A Flux Splitting Scheme with High Resolution and Robustness for Discontinuities," AIAA Paper 94-0083, Jan. 1994.

[15] Park, C., *Nonequilibrium Hypersonic Aerothermodynamics*, John Wiley and Sons, New York, 1989.

[16] Park, C., "Review of Chemical-Kinetic Problems of Future NASA Missions. 1: Earth Entries," *Journal of Thermophysics and Heat Transfer*, Vol. 7, No. 3, 1993, pp. 385–398.

[17] Park, C., Howe, J. T., Jaffe, R. L., and Candler, G. V., "Chemical-Kinetic Problems of Future NASA Missions. 2. Mars Entries: A Review," *Journal of Thermophysics and Heat Transfer*, Vol. 8, No. 1, 1994, pp. 9–23.

[18] Park, C., Jaffe, R. L., and Partridge, H., "Chemical-Kinetic Parameters of Hyperbolic Earth Entry," *Journal of Thermophysics and Heat Transfer*, Vol. 15, No. 1, 2001, pp. 76–90.

[19] Park, C., and Bogdanoff, D. W., "Shock-Tube Measurement of Nitridation Coefficient of Solid Carbon," *Journal of Thermophysics and Heat Transfer*, Vol. 20, No. 3, 2006, pp. 487–492.

[20] Blottner, F. G., "Prediction of Electron Density in the Boundary Layer on Entry Vehicles with Ablation," NASA SP-252, 1970, pp. 219–240.

[21] Blottner, F. G., Johnson, M., and Ellis, M., "Chemically Reacting Viscous Flow Program for Multi-Component Gas Mixture," Sandia National Lab., Rept. SC-RR-70-754, Albuquerque, NM, 1971.

[22] Vincenti, W. G., and Kruger, C. H., *Introduction to Physical Gas Dynamics*, Wiley, New York, 1967, pp. 375–435.

[23] Wilke, C. R., "A Viscosity Equation for Gas Mixture," *Journal of Chemical Physics*, Vol. 18, No. 4, 1950, pp. 517–519.

[24] Potts, R. L., "Application of Integral Methods to Ablation Charring Erosion, A Review," *Journal of Spacecraft and Rockets*, Vol. 32, No. 2, 1995, pp. 200–209.

[25] Zoby, E. V., "Empirical Stagnation-Point Heat-Transfer Relation in Several Gas Mixtures at High Enthalpy Levels," NASA TN D-4799, Oct. 1968.

[26] Metzger, J. W., Engel, M. J., and Diaconis, N. S., "Oxidation and Sublimation of Graphite in Simulated Re-entry Environments," *AIAA Journal*, Vol. 5, No. 3, 1967, pp. 451–460.